



BELLE2-CONF-PH-2022-018
November 9, 2022

Measurement of the photon-energy spectrum in inclusive $B \rightarrow X_s \gamma$ decays identified using hadronic decays of the recoil B meson in 2019–2021 Belle II data

(The Belle II Collaboration)

F. Abudinén, I. Adachi, K. Adamczyk, L. Aggarwal, P. Ahlburg, H. Ahmed, J. K. Ahn, H. Aihara, N. Akopov, A. Aloisio, F. Ameli, L. Andricek, N. Anh Ky, D. M. Asner, H. Atmacan, V. Aulchenko, T. Aushev, V. Aushev, T. Aziz, V. Babu, S. Bacher, H. Bae, S. Baehr, S. Bahinipati, A. M. Bakich, P. Bambade, Sw. Banerjee, S. Bansal, M. Barrett, G. Batignani, J. Baudot, M. Bauer, A. Baur, A. Beaubien, A. Beaulieu, J. Becker, P. K. Behera, J. V. Bennett, E. Bernieri, F. U. Bernlochner, V. Bertacchi, M. Bertemes, E. Bertholet, M. Bessner, S. Bettarini, V. Bhardwaj, B. Bhuyan, F. Bianchi, T. Bilka, S. Bilokin, D. Biswas, A. Bobrov, D. Bodrov, A. Bolz, A. Bondar, G. Bonvicini, A. Bozek, M. Bračko, P. Branchini, N. Braun, R. A. Briere, T. E. Browder, D. N. Brown, A. Budano, L. Burmistrov, S. Bussino, M. Campajola, L. Cao, G. Casarosa, C. Cecchi, D. Červenkov, M.-C. Chang, P. Chang, R. Cheaib, P. Cheema, V. Chekelian, C. Chen, Y. Q. Chen, Y. Q. Chen, Y.-T. Chen, B. G. Cheon, K. Chilikin, K. Chirapatpimol, H.-E. Cho, K. Cho, S.-J. Cho, S.-K. Choi, S. Choudhury, D. Cinabro, L. Corona, L. M. Cremaldi, S. Cunliffe, T. Czank, S. Das, N. Dash, F. Dattola, E. De La Cruz-Burelo, S. A. De La Motte, G. de Marino, G. De Nardo, M. De Nuccio, G. De Pietro, R. de Sangro, B. Deschamps, M. Destefanis, S. Dey, A. De Yta-Hernandez, R. Dhamija, A. Di Canto, F. Di Capua, S. Di Carlo, J. Dingfelder, Z. Doležal, I. Domínguez Jiménez, T. V. Dong, M. Dorigo, K. Dort, D. Dossett, S. Dreyer, S. Dubey, S. Duell, G. Dujany, P. Ecker, S. Eidelman, M. Eliachevitch, D. Epifanov, P. Feichtinger, T. Ferber, D. Ferlewicz, T. Fillinger, C. Finck, G. Finocchiaro, P. Fischer, K. Flood, A. Fodor, F. Forti, A. Frey, M. Friedl, B. G. Fulsom, M. Gabriel, A. Gabrielli, N. Gabyshev, E. Ganiev, M. Garcia-Hernandez, R. Garg, A. Garmash, V. Gaur, A. Gaz, U. Gebauer, A. Gellrich, J. Gemmler, T. Geßler, G. Ghevondyan, G. Giakoustidis, R. Giordano, A. Giri, A. Glazov, B. Gobbo, R. Godang, P. Goldenzweig, B. Golob, P. Gomis, G. Gong, P. Grace, W. Gradl, S. Granderath, E. Graziani, D. Greenwald, T. Gu, Y. Guan, K. Gudkova, J. Guillems, C. Hadjivasiliou, S. Halder, K. Hara, T. Hara, O. Hartbrich, K. Hayasaka, H. Hayashii, S. Hazra, C. Hearty, M. T. Hedges, I. Heredia de la Cruz, M. Hernández Villanueva, A. Hershenhorn, T. Higuchi, E. C. Hill, H. Hirata, M. Hoek, M. Hohmann, S. Hollitt, T. Hotta, C.-L. Hsu, K. Huang, T. Humair, T. Iijima, K. Inami, G. Inguglia, N. Ipsita, J. Irakkathil Jabbar, A. Ishikawa, S. Ito, R. Itoh, M. Iwasaki, Y. Iwasaki, S. Iwata, P. Jackson, W. W. Jacobs, D. E. Jaffe, E.-J. Jang, M. Jeandron, H. B. Jeon, Q. P. Ji, S. Jia, Y. Jin, C. Joo, K. K. Joo, H. Junkerkalefeld, I. Kadenko, J. Kahn, H. Kakuno, M. Kaleta, A. B. Kaliyar, J. Kandra, K. H. Kang, S. Kang, P. Kapusta, R. Karl, G. Karyan, Y. Kato, H. Kawai, T. Kawasaki,

C. Ketter, H. Kichimi, C. Kiesling, C.-H. Kim, D. Y. Kim, H. J. Kim, K.-H. Kim, K. Kim, S.-H. Kim, Y.-K. Kim, Y. Kim, T. D. Kimmel, H. Kindo, K. Kinoshita, C. Kleinwort, B. Knysh, P. Kodyš, T. Koga, S. Kohani, K. Kojima, I. Komarov, T. Konno, A. Korobov, S. Korpar, N. Kovalchuk, E. Kovalenko, R. Kowalewski, T. M. G. Kraetzschmar, F. Krinner, P. Križan, R. Kroeger, J. F. Krohn, P. Krokovny, H. Krüger, W. Kuehn, T. Kuhr, J. Kumar, M. Kumar, R. Kumar, K. Kumara, T. Kumita, T. Kunigo, M. Künzel, S. Kurz, A. Kuzmin, P. Kvasnička, Y.-J. Kwon, S. Lacaprara, Y.-T. Lai, C. La Licata, K. Lalwani, T. Lam, L. Lanceri, J. S. Lange, M. Laurenza, K. Lautenbach, P. J. Laycock, R. Leboucher, F. R. Le Diberder, I.-S. Lee, S. C. Lee, P. Leitl, D. Levit, P. M. Lewis, C. Li, L. K. Li, S. X. Li, Y. B. Li, J. Libby, K. Lieret, J. Lin, Z. Liptak, Q. Y. Liu, Z. A. Liu, D. Liventsev, S. Longo, A. Loos, A. Lozar, P. Lu, T. Lueck, F. Luetticke, T. Luo, C. Lyu, C. MacQueen, M. Maggiora, R. Maiti, S. Maity, R. Manfredi, E. Manoni, A. Manthei, S. Marcello, C. Marinas, L. Martel, A. Martini, T. Martinov, L. Massaccesi, M. Masuda, T. Matsuda, K. Matsuoka, D. Matvienko, J. A. McKenna, J. McNeil, F. Meggendorfer, F. Meier, M. Merola, F. Metzner, M. Milesi, C. Miller, K. Miyabayashi, H. Miyake, H. Miyata, R. Mizuk, K. Azmi, G. B. Mohanty, N. Molina-Gonzalez, S. Moneta, H. Moon, T. Moon, J. A. Mora Grimaldo, T. Morii, H.-G. Moser, M. Mrvar, F. J. Müller, Th. Muller, G. Muroyama, C. Murphy, R. Mussa, I. Nakamura, K. R. Nakamura, E. Nakano, M. Nakao, H. Nakayama, H. Nakazawa, A. Narimani Charan, M. Naruki, Z. Natkaniec, A. Natochii, L. Nayak, M. Nayak, G. Nazaryan, D. Neverov, C. Niebuhr, M. Niiyama, J. Ninkovic, N. K. Nisar, S. Nishida, K. Nishimura, M. H. A. Nouxman, K. Ogawa, S. Ogawa, S. L. Olsen, Y. Onishchuk, H. Ono, Y. Onuki, P. Oskin, F. Otani, E. R. Oxford, H. Ozaki, P. Pakhlov, G. Pakhlova, A. Paladino, T. Pang, A. Panta, E. Paoloni, S. Pardi, K. Parham, H. Park, S.-H. Park, B. Paschen, A. Passeri, A. Pathak, S. Patra, S. Paul, T. K. Pedlar, I. Peruzzi, R. Peschke, R. Pestotnik, F. Pham, M. Piccolo, L. E. Piilonen, G. Pinna Angioni, P. L. M. Podesta-Lerma, T. Podobnik, S. Pokharel, L. Polat, V. Popov, C. Praz, S. Prell, E. Prencipe, M. T. Prim, M. V. Purohit, H. Purwar, N. Rad, P. Rados, S. Raiz, A. Ramirez Morales, R. Rasheed, N. Rauls, M. Reif, S. Reiter, M. Remnev, I. Ripp-Baudot, M. Ritter, M. Ritzert, G. Rizzo, L. B. Rizzuto, M. Röhrken, S. H. Robertson, D. Rodríguez Pérez, J. M. Roney, C. Rosenfeld, A. Rostomyan, N. Rout, M. Rozanska, G. Russo, D. Sahoo, Y. Sakai, D. A. Sanders, S. Sandilya, A. Sangal, L. Santelj, P. Sartori, Y. Sato, V. Savinov, B. Scavino, M. Schnepf, M. Schram, H. Schreeck, J. Schueler, C. Schwanda, A. J. Schwartz, B. Schwenker, M. Schwickardi, Y. Seino, A. Selce, K. Senyo, I. S. Seong, J. Serrano, M. E. Seviar, C. Sfienti, V. Shebalin, C. P. Shen, H. Shibuya, T. Shillington, T. Shimasaki, J.-G. Shiu, B. Shwartz, A. Sibidanov, F. Simon, J. B. Singh, S. Skambraks, J. Skorupa, K. Smith, R. J. Sobie, A. Soffer, A. Sokolov, Y. Soloviev, E. Solovieva, S. Spataro, B. Spruck, M. Starič, S. Stefkova, Z. S. Stottler, R. Stroili, J. Strube, J. Stypula, Y. Sue, R. Sugiura, M. Sumihama, K. Sumisawa, T. Sumiyoshi, W. Sutcliffe, S. Y. Suzuki, H. Svidras, M. Tabata, K. Tackmann, M. Takahashi, M. Takizawa, U. Tamponi, S. Tanaka, K. Tanida, H. Tanigawa, N. Taniguchi, Y. Tao, P. Taras, F. Tenchini, R. Tiwary, D. Tonelli, E. Torassa, N. Toutounji, K. Trabelsi, I. Tsaklidis, T. Tsuboyama, N. Tsuzuki, M. Uchida, I. Ueda, S. Uehara, Y. Uematsu, T. Ueno, T. Uglov, K. Unger, Y. Unno, K. Uno, S. Uno, P. Urquijo, Y. Ushiroda, Y. V. Usov, S. E. Vahsen, R. van Tonder, G. S. Varner, K. E. Varvell, A. Vinokurova, L. Vitale, V. Vobbiliseti, V. Vorobyev, A. Vossen, B. Wach,

E. Waheed, H. M. Wakeling, K. Wan, W. Wan Abdullah, B. Wang, C. H. Wang, E. Wang, M.-Z. Wang, X. L. Wang, A. Warburton, M. Watanabe, S. Watanuki, J. Webb, S. Wehle, M. Welsch, C. Wessel, J. Wiechczynski, P. Wieduwilt, H. Windel, E. Won, L. J. Wu, X. P. Xu, B. D. Yabsley, S. Yamada, W. Yan, S. B. Yang, H. Ye, J. Yelton, J. H. Yin, M. Yonenaga, Y. M. Yook, K. Yoshihara, T. Yoshinobu, C. Z. Yuan, Y. Yusa, L. Zani, Y. Zhai, J. Z. Zhang, Y. Zhang, Y. Zhang, Z. Zhang, V. Zhilich, J. Zhou, Q. D. Zhou, X. Y. Zhou, V. I. Zhukova, V. Zhulanov, and R. Žlebčik

Abstract

We measure the photon-energy spectrum in radiative bottom-meson (B) decays into inclusive final states involving a strange hadron and a photon. We use SuperKEKB electron-positron collisions corresponding to 189 fb^{-1} of integrated luminosity collected at the $\Upsilon(4S)$ resonance by the Belle II experiment. The partner B candidates are fully reconstructed using a large number of hadronic channels. The $B \rightarrow X_s \gamma$ partial branching fractions are measured as a function of photon energy in the signal B meson rest frame in eight bins above 1.8 GeV. The background-subtracted signal yield for this photon energy region is 343 ± 122 events. Integrated branching fractions for three photon energy thresholds of 1.8 GeV, 2.0 GeV, and 2.1 GeV are also reported, and found to be in agreement with world averages.

1 Introduction

Flavour changing neutral currents (FCNCs) are only allowed in the Standard Model (SM) via loop processes and are therefore highly suppressed [1]. The $B \rightarrow X_s \gamma$ FCNC decays occur via radiative $b \rightarrow s$ transitions, where B denotes charged and neutral bottom-mesons, and X_s denotes all available final states containing net strangeness. These processes are particularly sensitive to non-SM effects [2]. In addition, their photon-energy spectrum offers access to various interesting parameters, such as the mass of the b quark and the function describing its motion inside the B meson [3, 4].

We present an inclusive measurement using $B \rightarrow X_s \gamma$ decays identified in $\Upsilon(4S) \rightarrow B\bar{B}$ events in which the partner B meson is reconstructed in its hadronic decays (hadronic tagging). This approach is complementary to the untagged or lepton-tagged (see e.g., [5]) and sum-of-exclusive (e.g., [6]) methods because it has different sources of systematic uncertainty. In addition, tagging provides a purer sample and the kinematic information from the partner- B meson gives direct access to observables in the signal- B meson rest frame. We denote the photon energy in the signal- B meson rest frame as E_γ^B . In this paper, the minimum E_γ^B photon energy threshold is 1.8 GeV. The inclusive analysis does not distinguish between contributions from $b \rightarrow d\gamma$ and $b \rightarrow s\gamma$ processes, therefore the much smaller $b \rightarrow d\gamma$ contribution is subtracted from the final results with a shape determined from simulation.

2 Belle II detector

The Belle II [7] detector is designed to reconstruct the final states of electron-positron collisions at center-of-mass energies at or near the $\Upsilon(4S)$ meson mass. The colliding e^+e^- beams are provided by the SuperKEKB collider [8] at KEK in Tsukuba, Japan. The detector has collected physics data since 2019. Belle II consists of several detector subsystems arranged cylindrically around the beam pipe. In the Belle II coordinate system, the x axis is defined to be horizontal and points to the outside of the tunnel for the accelerator's main rings, the y axis is vertically upward, and the z axis is defined in the direction of the electron beam. The azimuthal angle, ϕ , and the polar angle, θ , are defined with respect to the z axis. Three regions in the detector are defined based on θ : forward endcap ($12^\circ < \theta < 31^\circ$), barrel ($32^\circ < \theta < 129^\circ$) and backward endcap ($131^\circ < \theta < 155^\circ$).

The Belle II vertex detector is designed to precisely determine particle decay vertices. It is the innermost subsystem, and consists of a silicon pixel detector and a silicon strip detector. Surrounding the vertexing subsystems is the central drift chamber, which is used to measure charged-particle trajectories (tracks) to determine their charge and momentum. It also provides important particle-identification information by measuring the specific ionisation of charged tracks. Further particle identification is provided by the time-of-propagation detector and the aerogel ring-imaging Cherenkov detector, which cover, respectively, the barrel and the forward endcap regions of Belle II. Photons and electrons are stopped and their energy deposits (clusters) are read out by the CsI(Tl)-crystal electromagnetic calorimeter. The photon-energy resolution of the ECL is better than 20 MeV for photons above 1 GeV. All the inner components are surrounded by a superconducting solenoid, which provides a uniform axial 1.5 T magnetic field. The K_L^0 and muon detector, composed of plastic scintillators and resistive-plate chambers, is the outermost subsystem of Belle II.

3 Data sets

The results presented here use a data sample corresponding to 189 fb^{-1} of integrated luminosity collected at an energy corresponding to the $\Upsilon(4S)$ mass. In addition, an off-resonance data set corresponding to 18 fb^{-1} collected 60 MeV below the $\Upsilon(4S)$ resonance is used to validate the $e^+e^- \rightarrow q\bar{q}$ simulation. Here q is used to indicate u , d , s and c quarks.

The relevant background and signal processes are modeled using large samples simulated through the Monte Carlo (MC) method corresponding to 1.6 ab^{-1} of $e^+e^- \rightarrow q\bar{q}$ events (generated by KKMC [9], interfaced to PYTHIA [10]) and $\Upsilon(4S) \rightarrow B^0\bar{B}^0, B^+B^-$ events (generated by EVTGEN [11]). The detector response is simulated using Geant 4 [12].

In addition, inclusive $B \rightarrow X_s\gamma$ signal distributions are generated using BTOXSGAMMA, the EVTGEN implementation of the Kagan-Neubert model [13], with values of the model parameters taken from Ref. [4]. The inclusive model, by construction, does not reproduce the resonant structure of the $b \rightarrow s\gamma$ transitions. Therefore, the $B \rightarrow K^*(892)\gamma$ sample (later denoted as $B \rightarrow K^*\gamma$) generated by EVTGEN is also used, as it dominates the higher end of the E_γ spectrum. The $B \rightarrow X_s\gamma$ and $B \rightarrow K^*\gamma$ signal simulations are combined using a “hybrid-model”, inspired by Ref. [14]. The full spectrum is modelled by the combination of the two simulated signal samples. A set of hybrid E_γ^B intervals (bins) is defined and the $B \rightarrow X_s\gamma$ spectrum is scaled in each bin to match the partial branching fraction of the combined $B \rightarrow X_s\gamma$ and $B \rightarrow K^*\gamma$ decays with the expected value. The hybrid signal model is used in the selection optimisation, efficiency determination, and unfolding procedure.

All the data sets are analysed using the Belle II analysis software framework [15].

4 Analysis overview

A sample of tagged B mesons is first reconstructed in their hadronic decays, and a high-energy photon from the other B meson is selected. Details of the tagging algorithm are described in Section 5.1. The selection procedures to suppress photon candidates from background processes are given in Sections 5.2 and 5.3. They are optimised in simulation, simultaneously, by maximising the figure of merit of Ref. [16]. The final best tag-candidate selection is summarised in Section 5.4. The fitting of sample composition is described in Section 6. The procedure to remove the remaining background contamination after the fit is given in Section 7. The reconstructed $B \rightarrow X_s\gamma$ event yields in bins of E_γ^B are unfolded (Section 8). The corresponding uncertainties are discussed in Section 9. The final results of the analysis are presented in Section 10.

The analysis is fully optimised on simulation. Control regions are used to check the validity of the background suppression before examining the signal region.

5 Event reconstruction and selection

5.1 Tag side reconstruction

In each event, one B meson candidate is fully reconstructed and used as a tag for the recoiling signal B meson candidate. The tag-side B meson is reconstructed using the full-event-interpretation algorithm (FEI) [17], which reconstructs hadronic B decays from thousands of subdecay chains. The algorithm starts by combining track and ECL cluster information to reconstruct final-state candidate particles, such as electrons, muons, photons, charged

pions, and kaons. In the next step, those are combined to form intermediate particles such as π^0 , K_S^0 , $D^{(*)}$, and J/ψ candidates. The intermediate or final-state particles are combined to form B candidates in 36 B^+ and 32 B^0 hadronic modes. For each reconstructed B -meson candidate, the algorithm outputs a probability-like score, \mathcal{P}_{FEI} . Correctly reconstructed B -meson candidates have a score close to one, whereas non- B and misreconstructed candidates tend to have a score close to zero.

For tag-candidate reconstruction, track-quality requirements are imposed [18]. The longitudinal distance of closest approach of each track from the detector center is required to be $|z_0| < 2.0$ cm. A similar criterion for the distance in the transverse plane, $|d_0| < 0.5$ cm is also applied. Only charged particles with transverse momenta, p_T , higher than 0.1 GeV/ c are selected. Furthermore, an event must have at least three tracks passing these selections. Similarly, three or more isolated clusters with $17 < \theta < 150^\circ$ and $E > 0.1$ GeV are required in the ECL for each event. The total energy deposited in the ECL should be within 2 and 7 GeV. Only events with at least 4 GeV of measured energy in the Belle II detector are retained. The tag-side B candidates are required to have $\mathcal{P}_{\text{FEI}} > 0.001$ and beam-constrained mass, $M_{\text{bc}} > 5.245$ GeV/ c^2 , defined as

$$M_{\text{bc}} = \sqrt{(\sqrt{s}/2)^2 - p_{\text{tag}}^2}, \quad (1)$$

where \sqrt{s} is the collision energy and p_{tag} is the reconstructed momentum of the tag-candidate in the CM frame. Furthermore, a $|\Delta E| < 0.2$ GeV requirement is imposed on the energy difference, defined as

$$\Delta E = E_{\text{tag}} - \sqrt{s}/2, \quad (2)$$

where E_{tag} is the energy of the tag-candidate reconstructed in the CM frame.

5.2 Signal-side selection

Using the kinematic properties of the reconstructed tag-side meson and the beam-energy constraint, the photon-candidate energy is inferred in the signal- B meson rest-frame. All candidates in the range of $E_\gamma^B > 1.4$ GeV are considered. The highest-energy photon in each event is taken as the signal-photon candidate. Studies on simulated signal events show that this selects the correct $B \rightarrow X_s \gamma$ candidate in more than 99% of cases. Cluster-timing information, derived from a waveform fit to the signal collected in the most energetic crystal of the cluster, is associated to each photon. In order to suppress the large background from out-of-time beam-background clusters or photons associated with low-quality waveform fits, the cluster timing, measured with respect to the collision time, is used. It is required neither to exceed 200 ns nor twice the cluster-time uncertainty. This selection introduces about a 2% signal efficiency loss while reducing beam background to negligible levels.

The resulting sample is dominated by photon candidates originating from asymmetric $\pi^0 \rightarrow \gamma\gamma$ and $\eta \rightarrow \gamma\gamma$ decays. This background is suppressed by vetoing π^0 and η decays. Signal-photon candidates are kinematically combined with lower-energy photons in the event and a quantitative measure of compatibility with $\pi^0 \rightarrow \gamma\gamma$ or $\eta \rightarrow \gamma\gamma$ decays is associated to the combinations. The compatibility is determined using a multivariate statistical-learning algorithm that uses the diphoton invariant mass, helicity, and properties of the less-energetic photon, such as energy, polar angle, and smallest ECL cluster-to-track distance. Another statistical-learning algorithm uses Zernike moments to quantify the ECL-photon cluster shape

to disentangle misidentified photons from signal clusters. The background suppression of these selections is investigated using the off-resonance data. Furthermore, samples with inverted π^0 and η suppression requirements are used to form large samples of background-like events.

5.3 Suppression of $q\bar{q}$ events

Photon candidates from background $e^+e^- \rightarrow q\bar{q}$ events make up most of the selected sample. A dedicated boosted-decision-tree classifier is trained to suppress these events. The training is performed on randomly selected sets of 10^5 simulated $q\bar{q}$ events and 10^5 simulated $B \rightarrow X_s\gamma$ events that pass the requirements described in Sections 5.1 and 5.2. The input features for the classifier are tag-side B kinematic parameters, such as modified Fox-Wolfram moments [19], B decay vertex parameters, CLEO cones [20], and thrust [21]. For each variable, we require minimal correlations with E_γ^B and M_{bc} in order not to bias the inclusive spectrum. Furthermore, each variable distribution in off-resonance data is compared to $e^+e^- \rightarrow q\bar{q}$ simulation. Only those showing good data-simulation agreement are used for the training. The classifier outputs a probability score, \mathcal{P}_{BDT} , for each event to be classified as $e^+e^- \rightarrow q\bar{q}$ or $e^+e^- \rightarrow B\bar{B}$ where one of the B mesons decays as $B \rightarrow X_s\gamma$.

5.4 Best tag-side candidate selection

After all the selections described in Section 5, about 50% of events have a unique tag-side candidate, based on the hybrid signal model. In 25% of cases there are two tag-side candidates remaining, and in 10% of cases – three. The probability to have more than one tag-side candidate decreases rapidly and is lower than 1% for 5 or more candidates. If more than one tag-side candidate is present in an event, only the one with the highest \mathcal{P}_{FEI} is retained.

5.5 Selection efficiency

The signal efficiency is decomposed as a product of the FEI tagging efficiency and the signal-selection efficiency. Signal-selection and tagging efficiencies are calculated using the simulated hybrid model. The tagging efficiencies are calculated by comparing B yields in simulation before and after the FEI algorithm is applied. After applying the FEI calibration factors of $\mathcal{C}_{B^+} = 0.66 \pm 0.02$ and $\mathcal{C}_{B^0} = 0.67 \pm 0.02$ for charged and neutral modes, respectively, a tagging efficiency of $(0.44 \pm 0.02)\%$ is found. The calibration factors account for differences in the tag-side reconstruction efficiency between data and simulation and are derived in an independent study of hadronic-tagged $B \rightarrow X\ell\nu$ decays [22]. The signal-selection efficiency is calculated as the fraction of tagged-signal yield that meet the requirements of Section 5.2. It increases approximately linearly from 45% to 63% with $E_\gamma^B \in [1.8, 2.6]$ GeV, with a total uncertainty of about 10% in each bin. Background events from $e^+e^- \rightarrow q\bar{q}$ are suppressed by 99.5%, while the generic $e^+e^- \rightarrow B\bar{B}$ background is reduced by 93%.

6 Fit of sample composition

The tag-side M_{bc} distribution is fit to determine the yields of B mesons that provide good kinematic constraints on the signal side, the remaining $q\bar{q}$ events, and combinatorial $B\bar{B}$

events. The sample is divided in 11 bins of E_γ^B : three 200-MeV-wide bins for the 1.4–2.0 GeV range; seven 100-MeV-wide bins for the 2.0–2.7 GeV region; and a single $E_\gamma^B > 2.7$ GeV bin. The first two bins and the last one are chosen as control regions for the fit due to expected large background or low signal yield. The signal region is therefore defined as $1.8 < E_\gamma^B < 2.7$ GeV.

The model for the fit of sample composition is determined using simulation. The simulated sample is split into three components: correctly reconstructed (peaking) $B\bar{B}$ events, $q\bar{q}$ decays, and combinatorial background from $B\bar{B}$ decays. ‘Peaking’ henceforth is used generically to denote the resonant behaviour in M_{bc} of correctly reconstructed tag-side B decays. These components have distinct shapes in M_{bc} , which are parameterised using probability distribution functions (PDFs). To extract the yield of peaking $B\bar{B}$ tags, a Crystal Ball function is used [23]. This function is the sum of a peaking Gaussian part and a polynomial tail. The $q\bar{q}$ decays are described by an ARGUS function [24]. Combinatorial $B\bar{B}$ background is described by a fifth-order Chebyshev polynomial. Studies on simulation show that a lower-order polynomial is insufficient to accurately describe the M_{bc} shape of this component.

Likelihood fits to the unbinned M_{bc} distributions are performed simultaneously in the E_γ^B bins [25]. A modeling fit is performed on separate components in simulated data to determine the shape parameters and fix them. The fit is then applied to the experimental data. The yields of the three components in each E_γ^B interval, and the ARGUS shape parameters – which are shared across bins – are determined by the fit (Figure 1). The peaking- B yields in each E_γ^B bin are extracted from the Crystal-Ball normalizations. The peaking- B yield estimator is unbiased and has Gaussian uncertainties as shown by checks on simplified simulated experiments.

7 Residual B background subtraction

The resulting peaking B yields include contributions from $B \rightarrow X_{s+d}\gamma$ events and other correctly-tagged $B\bar{B}$ processes, which are considered background. Due to the high-purity of the tagged sample, background contamination is low at high- E_γ^B , but grows sharply with decreasing E_γ^B .

To remove this background, the PDFs defined in Section 6 are used to fit simulated $B\bar{B}$ samples in which $B \rightarrow X_{s+d}\gamma$ events are removed. This procedure extracts yields of peaking nonsignal events in every E_γ^B bin. The background predictions are scaled for luminosity, and corrected based on FEI calibration factors [22], γ detection-efficiency [26], and π^0 efficiency. Branching fractions used in simulation for the background modes are matched to the most recent known values. The $1.4 < E_\gamma^B < 1.8$ GeV region, where signal purity is low, is used for validating the background subtraction. Event yields observed in data after subtraction are compared with expectations from background-only simulation. An 8.7% difference is observed, which is assigned as a uniform correction factor for background normalisation across bins. The background expectations from simulation and observed yields in data are shown in Figure 2.

8 Unfolding

The measured $B \rightarrow X_s\gamma$ spectrum needs to be corrected (unfolded) for smearing effects. The unfolding uses bin-by-bin multiplicative factors based on the hybrid model. These factors

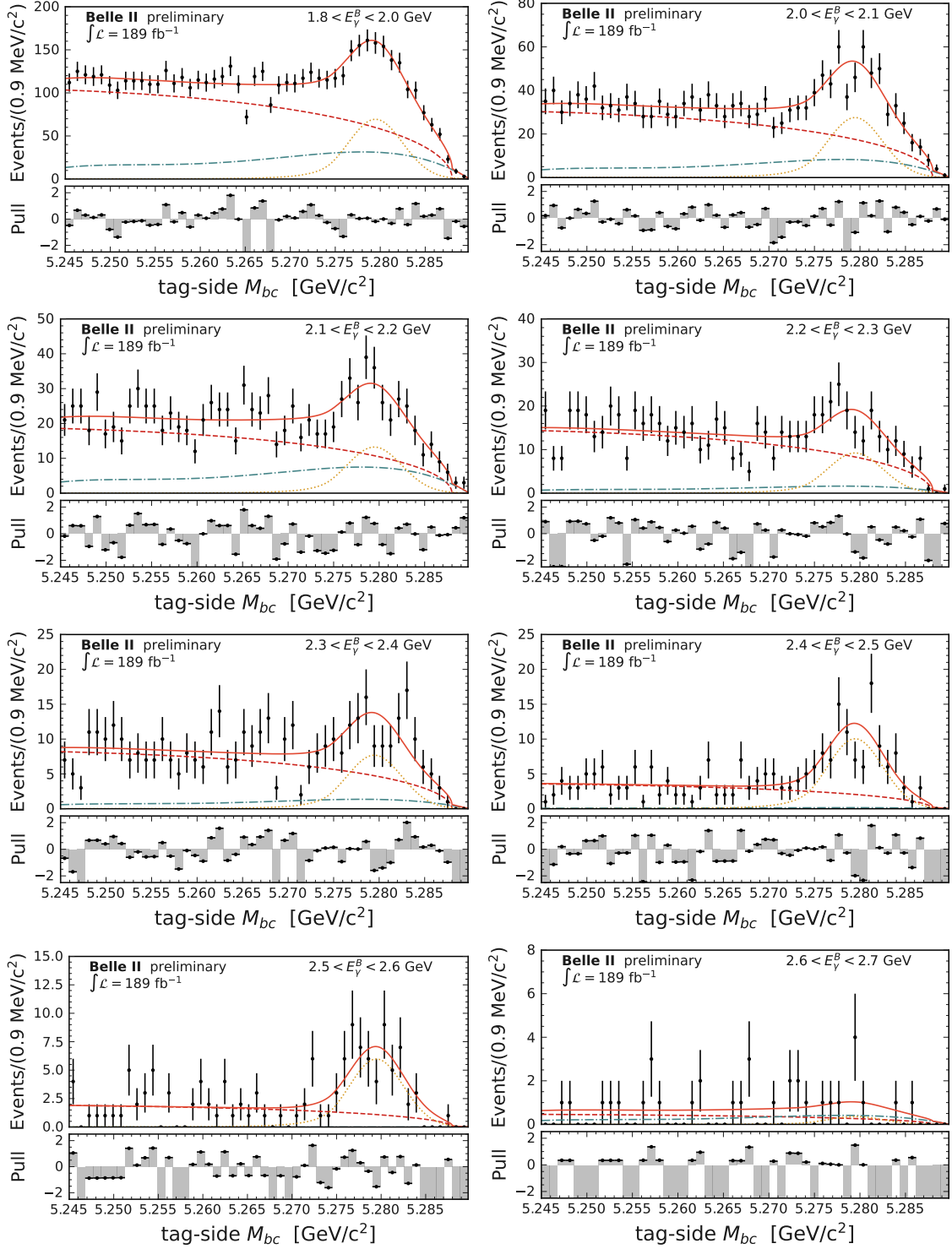


FIG. 1: Distributions of (black markers with error bars) beam-constrained mass for tag-side B meson candidates restricted to eight E_γ^B bins, with (curves) fit projections overlaid. The orange dotted curve corresponds to the $B\bar{B}$ peaking tags. The dashed and dash-dotted curves correspond to the $q\bar{q}$ and misreconstructed $B\bar{B}$ components, modelled by ARGUS and Chebyshev PDFs, respectively. The solid red curve corresponds to the total fit. The lower panels show the difference between fit results and measured values, divided by its statistical uncertainty (pull).

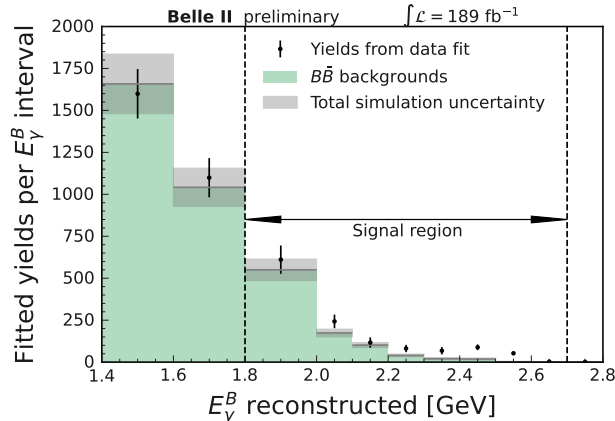


FIG. 2: Yield of $B\bar{B}$ events as a function of photon energy in the signal B meson rest frame. The data points correspond to the yields from the fits on the data M_{bc} distributions. The histogram shows the luminosity-scaled yields from the background-only simulated sample. The gray bands correspond to systematic uncertainties on the $B\bar{B}$ background prediction. The excess of events in data with respect to the $B\bar{B}$ background is the $B \rightarrow X_{s+d}\gamma$ contribution.

are defined as the ratios between the expected number of events of the generated spectrum and the expected number of corresponding events of the reconstructed spectrum within an E_γ^B interval. The measured $B \rightarrow X_s\gamma$ yields are multiplied by the unfolding factors (see Section 10). The bulk of the unfolding factors do not exceed 10-20%, and only the edge bins have 30-60% corrections.

9 Uncertainties

Multiple sources of systematic uncertainty are considered and are grouped as follows: uncertainties due to assumptions in the fit; uncertainties affecting the signal efficiency estimation; data-MC normalisation in the background estimation; and other sources, such as unfolding procedure, branching fraction normalization and the subtraction of $B \rightarrow X_d\gamma$ component. The statistical uncertainties of the yields extracted from the fit on data are dominant.

9.1 Uncertainties due to assumptions in the fit

To account for assumptions on the values of model parameters, we repeat the fits by varying the Chebyshev polynomial coefficients by their one-standard-deviation uncertainties, and take the maximum shift in signal yield as the uncertainty. We account for a known data-simulation mismodelling of the M_{bc} endpoint due to non-simulated run-dependant variations of the collision energy. The signal yields observed in data using alternative models of background shapes with various M_{bc} endpoints are compared. The maximum variation with respect to the central result is taken as uncertainty.

9.2 Signal efficiency uncertainties

The signal efficiency is calculated using the simulated hybrid-model signal sample. The values are corrected using FEI simulation-to-data calibration factors, \mathcal{C}_{B^0/B^+} [22], as well as

acceptance corrections from the π^0 veto and γ efficiency. The corresponding uncertainties related to these factors are propagated as systematic uncertainties. The signal efficiency is validated in the high-purity $E_\gamma^B \in [2.5, 2.6]$ GeV region, and the observed difference assigned as an uncertainty.

9.3 Background uncertainties

The uncertainties associated with the limited size of the simulated samples used in the M_{bc} fits are propagated to the final results. Similarly to the signal efficiency, the background yields extracted from the fits on simulated samples are corrected using FEI calibration, π^0 veto efficiency, and γ detection-efficiency correction factors. Uncertainties on the branching fractions of background decay modes are also included. The observed background-normalisation difference (see Section 7) is assigned as a 100% systematic uncertainty.

9.4 Other uncertainties

To unfold the measured E_γ^B spectrum, we evaluate the hybrid-model shape uncertainties by taking into account the uncertainty on the ratio of the known branching fractions of $B \rightarrow K^*\gamma$ to that of $B \rightarrow X_s\gamma$. The $B \rightarrow X_s\gamma$ model-parameter uncertainties, based on Ref. [4], are also included. The analysis does not distinguish between X_s and X_d final-states. The contribution from the $B \rightarrow X_d\gamma$ component is subtracted assuming the same shape and selection efficiency as $B \rightarrow X_s\gamma$. Under this assumption, the $\mathcal{B}(B \rightarrow X_s\gamma)$ and $\mathcal{B}(B \rightarrow X_d\gamma)$ ratio equals $|V_{td}/V_{ts}|^2$. The full size of the $B \rightarrow X_d\gamma$ component is assigned as an uncertainty. The uncertainty on the number of B meson pairs, used as the branching-fraction normalization, is also taken into account. It is estimated by an independent study with a data-driven method in which off-resonance data are used to subtract the non- $B\bar{B}$ contribution from the on-resonance data.

10 Results

The partial branching fractions in the various E_γ^B intervals are calculated as

$$\frac{1}{\Gamma_B} \frac{d\Gamma_i}{dE_\gamma^B} = \frac{\mathcal{U}_i \times (N_i^{\text{DATA}} - N_i^{\text{BKG, MC}} - N_i^{B \rightarrow X_d\gamma})}{\varepsilon_i \times N_B}, \quad (3)$$

where

- N_i^{DATA} is the peaking- B yield extracted from fitting the data distributions,
- $N_i^{\text{BKG, MC}}$ is the non- $B \rightarrow X_{s+d}\gamma$ peaking- B yield expectation extracted from fitting simulated distributions, scaled for luminosity and corrected as discussed in Section 7,
- $N_i^{B \rightarrow X_d\gamma}$ is the number of $B \rightarrow X_d\gamma$ events, equal to $|V_{td}/V_{ts}|^2 \approx 4.3\%$ [27] of $N_i^{B \rightarrow X_s\gamma}$, assuming the same shape and selection efficiency as $B \rightarrow X_s\gamma$,
- ε_i is the $B \rightarrow X_s\gamma$ selection and tagging efficiency, calculated using the simulated hybrid-model sample,
- \mathcal{U}_i is the bin-by-bin unfolding factor calculated using the simulated hybrid-model sample,

- $N_B \equiv 2 \times (198 \pm 3) \times 10^6$ is the number of B mesons in the 189 fb^{-1} data sample,
- Γ_B on the left-hand-side of Equation 3 signifies the total decay width of the B -meson.

The resulting partial branching fractions are shown in Figure 3. The various contributions from the major sources of systematic uncertainties as functions of E_γ^B are shown in Table I.

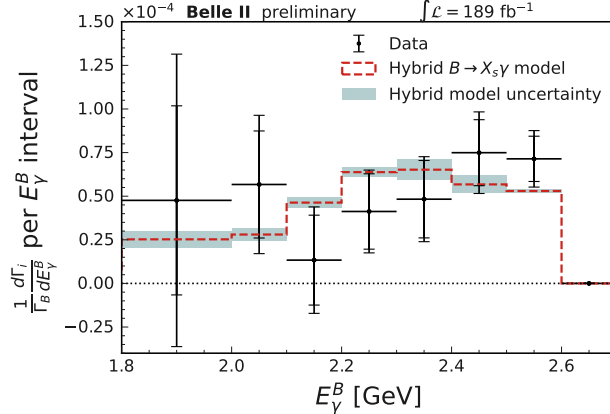


FIG. 3: Measured partial branching fractions $(1/\Gamma_B)(d\Gamma_i/dE_\gamma^B)$ as a function of E_γ^B . The outer (inner) uncertainty bar shows the total (statistical) uncertainty. The overlaid model and uncertainty corresponds to the hybrid model.

TABLE I: Results of the partial branching fraction measurements. The right-hand part of the table shows the main contributions to the systematic uncertainty. Signal efficiency and background modelling uncertainties are correlated (see Sections 9.2 and 9.3).

E_γ^B [GeV]	$\frac{1}{\Gamma_B} \frac{d\Gamma_i}{dE_\gamma^B} (10^{-4})$	Statistical	Systematic	Fit procedure	Signal efficiency	Background modelling	Other
1.8 – 2.0	0.48	0.54	0.64	0.42	0.03	0.49	0.09
2.0 – 2.1	0.57	0.31	0.25	0.17	0.06	0.17	0.07
2.1 – 2.2	0.13	0.26	0.16	0.13	0.01	0.11	0.01
2.2 – 2.3	0.41	0.22	0.10	0.07	0.05	0.04	0.02
2.3 – 2.4	0.48	0.22	0.10	0.06	0.06	0.02	0.05
2.4 – 2.5	0.75	0.19	0.14	0.04	0.09	0.02	0.09
2.5 – 2.6	0.71	0.13	0.10	0.02	0.09	0.00	0.04

The integrated branching ratios for various E_γ^B thresholds are calculated and shown in Table II. The systematic uncertainties are computed taking the bin-by-bin correlations into account.

11 Conclusion

We present a measurement of the photon-energy spectrum in the B meson rest frame from $B \rightarrow X_s \gamma$ decays using hadronic-tagging of the partner B meson. We also report the

TABLE II: Integrated partial branching fractions for three E_γ^B thresholds. The number of observed events before unfolding and efficiency corrections are also given for each threshold.

E_γ^B threshold [GeV]	$\mathcal{B}(B \rightarrow X_s \gamma)$ [10^{-4}]	Observed signal yield (tot. unc.)
1.8	3.54 ± 0.78 (stat.) ± 0.83 (syst.)	343 ± 122
2.0	3.06 ± 0.56 (stat.) ± 0.47 (syst.)	285 ± 68
2.1	2.49 ± 0.46 (stat.) ± 0.35 (syst.)	219 ± 50

inclusive branching ratio $\mathcal{B}(B \rightarrow X_s \gamma)$ for various thresholds, starting at $E_\gamma^B > 1.8$ GeV. The results are consistent with the Standard Model and world averages [28].

Acknowledgments

We thank the SuperKEKB group for the excellent operation of the accelerator; the KEK cryogenics group for the efficient operation of the solenoid; and the KEK computer group for on-site computing support.

-
- [1] M. Misiak, A. Rehman and M. Steinhauser, *Towards $\bar{B} \rightarrow X_s \gamma$ at the NNLO in QCD without interpolation in m_c* , *J. High Energy Phys.* **06** (2020) 175 [2002.01548].
 - [2] M. Misiak and M. Steinhauser, *Weak radiative decays of the B meson and bounds on M_{H^\pm} in the Two-Higgs-Doublet Model*, *Eur. Phys. J. C* **77** (2017) 201 [1702.04571].
 - [3] J. Dingfelder and T. Mannel, *Leptonic and semileptonic decays of B mesons*, *Rev. Mod. Phys.* **88** (2016) 035008.
 - [4] SIMBA COLLABORATION, *Precision Global Determination of the $B \rightarrow X_s \gamma$ Decay Rate*, *Phys. Rev. Lett.* **127** (2021) 102001 [2007.04320].
 - [5] BABAR COLLABORATION, *Precision Measurement of the $B \rightarrow X_s \gamma$ Photon Energy Spectrum, Branching Fraction, and Direct CP Asymmetry $A_{CP}(B \rightarrow X_{s+d} \gamma)$* , *Phys. Rev. Lett.* **109** (2012) 191801 [1207.2690].
 - [6] BELLE COLLABORATION, *Measurement of the $\bar{B} \rightarrow X_s \gamma$ Branching Fraction with a Sum of Exclusive Decays*, *Phys. Rev. D* **91** (2015) 052004 [1411.7198].
 - [7] BELLE II COLLABORATION, *Belle II Technical Design Report*, 1011.0352.
 - [8] SUPERKEKB COLLABORATION, *SuperKEKB Collider*, *Nucl. Instrum. Meth. A* **907** (2018) 188 [1809.01958].
 - [9] B.F.L. Ward, S. Jadach and Z. Was, *Precision calculation for $e^+e^- \rightarrow 2f$: The KK MC project*, *Nucl. Phys. B Proc. Suppl.* **116** (2003) 73 [hep-ph/0211132].
 - [10] T. Sjostrand, S. Mrenna and P.Z. Skands, *A Brief Introduction to PYTHIA 8.1*, *Comput. Phys. Commun.* **178** (2008) 852 [0710.3820].
 - [11] A. Ryd, D. Lange, N. Kuznetsova, S. Versille, M. Rotondo, D.P. Kirkby et al., *EvtGen: A Monte Carlo Generator for B-Physics*, Tech. Rep. (May, 2005).
 - [12] GEANT4 COLLABORATION, *GEANT4: A Simulation toolkit*, *Nucl.Instrum.Meth.* **A506** (2003) 250.

- [13] A.L. Kagan and M. Neubert, *QCD anatomy of $B \rightarrow X_s \gamma$ decays*, *Eur. Phys. J. C* **7** (1999) 5 [hep-ph/9805303].
- [14] C. Ramirez, J.F. Donoghue and G. Burdman, *Semileptonic $b \rightarrow u$ decay*, *Phys. Rev. D* **41** (1990) 1496.
- [15] BELLE-II FRAMEWORK SOFTWARE GROUP, *The Belle II Core Software*, *Comput. Softw. Big Sci.* **3** (2019) 1 [1809.04299].
- [16] G. Punzi, *Sensitivity of searches for new signals and its optimization*, *eConf C030908* (2003) MODT002 [physics/0308063].
- [17] T. Keck et al., *The Full Event Interpretation: An Exclusive Tagging Algorithm for the Belle II Experiment*, *Comput. Softw. Big Sci.* **3** (2019) 6 [1807.08680].
- [18] BELLE II TRACKING GROUP, *Track finding at Belle II*, *Comput. Phys. Commun.* **259** (2021) 107610 [2003.12466].
- [19] BELLE COLLABORATION, *Evidence for $B^0 \rightarrow \pi^0 \pi^0$* , *Phys. Rev. Lett.* **91** (2003) 261801 [hep-ex/0308040].
- [20] CLEO COLLABORATION, *Search for exclusive charmless hadronic B decays*, *Phys. Rev. D* **53** (1996) 1039 [hep-ex/9508004].
- [21] BABAR, BELLE COLLABORATION, *The Physics of the B Factories*, *Eur. Phys. J. C* **74** (2014) 3026 [1406.6311].
- [22] BELLE II COLLABORATION, *A calibration of the Belle II hadronic tag-side reconstruction algorithm with $B \rightarrow X \ell \nu$ decays*, 2008.06096.
- [23] T. Skwarnicki, *A study of the radiative CASCADE transitions between the Upsilon-Prime and Upsilon resonances*, Ph.D. thesis, Cracow, INP, 1986.
- [24] H. Albrecht et al., *Search for hadronic $b \rightarrow u$ decays*, *Phys. Lett. B* **241** (1990) 278.
- [25] J. Eschle, A. Puig Navarro, R. Silva Coutinho and N. Serra, *zfit: scalable pythonic fitting*, *SoftwareX* **11** (2020) 100508 [1910.13429].
- [26] BELLE II COLLABORATION, *Measurement of the data to MC ratio of photon reconstruction efficiency of the Belle II calorimeter using radiative muon pair events*, Tech. Rep. BELLE2-NOTE-PL-2021-008 (Sep, 2021).
- [27] PARTICLE DATA GROUP, *Review of Particle Physics*, *Prog. Theor. Exp. Phys.* **2022** (2022) 083C01.
- [28] Y. Amhis et al., *Averages of b -hadron, c -hadron, and τ -lepton properties as of 2021*, 2206.07501.